Arch. Mech., **52**, 4–5, pp. 799–815, Warszawa 2000

# Fatigue crack evolution in a metal reinforced by short fibres

*Dedicated to Professor Zenon Mróz*
*on the occasion of his $70^{th}$ birthday*

V. TVERGAARD and T. Ø. PEDERSEN[1]

*Department of Solid Mechanics*
*Technical University of Denmark*
*DK-2800 Kgs. Lyngby, Denmark*

IN NUMERICAL ANALYSES OF FATIGUE damage evolution in metal matrix composites, the development of final failure and the subsequent crack growth in the material are accounted for. Cell model analyses are used for aluminium reinforced by short SiC fibres, with the matrix material represented by a cyclic plasticity model, in which continuum damage mechanics is incorporated to model fatigue damage. The Bauschinger effect, ratchetting, mean stress relaxation, and cyclic hardening or softening can be accounted for by the material model, as is important in studies of low cycle fatigue. Different fibre aspect ratios and spacings are studied for different loading cases.

## 1. Introduction

AN INCREASE OF THE TENSILE STRENGTH and the stiffness of a metal can be obtained by a reinforcement using short brittle fibres. However, such reinforcement also leads to poor ductility and low fracture toughness. The failure mechanisms for such metal matrix composites under monotonic loading can be divided in three groups: ductile matrix failure, debonding of the matrix-fibre interface, and brittle failure of the reinforcements, as has been discussed by NEEDLEMAN *et al.* [1]. For these failure mechanisms, numerical cell model studies are well suited to obtain a parametric understanding of the effect of different material parameters, such as the fibre volume fraction, the shape and distribution of fibres, and the matrix parameters (NUTT and NEEDLEMAN [2], TVERGAARD [3, 4, 5, 6], LLORCA *et al.* [7]).

For cyclic loading, where fatigue failure or even ratchetting can develop, ALLISON and JONES [8] have reviewed experimental results on the behaviour of

[1]Present address: MAN B&W Diesel A/S, Research and Development, Teglholmsgade 41, DK-2450 København SV, Denmark

discontinuously reinforced metal matrix composities (MMC), in particular aluminium based composites. Both the matrix fatigue damage, and the effect of particle fracture and debonding at the particle-matrix interface are described in [8]. It is emphasized that the plastic strain range during cycling is the predominant factor influencing fatigue damage, and that it is important to distinguish between average strains and local strains due to the highly nonuniform straining in the two-phase materials. Experiments by LLORCA and POZA [9] for SiC particulate reinforced Al have focussed on effects of reinforcement fracture. Analyses by LLORCA *et al.* [10], using the GURSON model [11] for MMC's under cyclic loading, consider the first 9 cycles and find agreement with some of the damage features observed experimentally. However, the Gurson material model with isotropic hardening does not account for a number of important cyclic plasticity effects.

The present investigation follows the approach used by the authors [12, 13] in studies of the initial damage development for low-cycle fatigue in MMC's. These analyses are here extended to also account for final failure leading to crack formation in the matrix material. Cyclic plasticity in metals can be described by various more complex material models such as the fraction model of BESSELING [14] or the multisurface kinematic hardening model of MRÓZ [15]. The description here is based on a nonlinear kinematic hardening rule (ARMSTRONG and FREDERICK [16], LEMAITRE and CHABOCHE [17]), using a superposition of isotropic hardening and kinematic hardening, for which it has been found that the Bauschinger effect, cyclic hardening or softening, ratchetting, and mean stress relaxation can be described. With continuum damage added to this model (LEMAITRE [18]), fatigue damage evolution can be described, and the particular fatigue model to be used here has been employed by PEDERSEN [19, 20] to study fatigue failure in cold-forging tools. A similar model has been used in [21] to study the creep-fatigue interaction.

Only the matrix fatigue failure is considered in the present study, so that perfect bonding is assumed between the matrix and fibres, and the possibility of fibre fracture is neglected. However, with short fibre reinforcement plastic yielding in the matrix starts early, and there is a wide range of cyclic loads for which fatigue life is mainly controlled by the matrix fatigue characteristics [8].

It should be noted that a damage model directly based on the micromechanics of the failure mechanism would be preferable, but such a model for growing microcrack density during cyclic plasticity has not been developed. Also, the continuum damage model with a single scalar damage parameter cannot describe the orientation effects associated with microcracks. However, a number of studies of low cycle fatigue in structural components have shown that the model has good predictive abilities.

## 2. Problem formulation and material model

The evolution of fatigue damage and fatigue crack formation in a metal reinforced by short fibres is here studied by analysing a unit cell containing a single fibre. The material with the periodic array of aligned fibres shown in Fig. 1 is modelled approximately by an axisymmetric cell model proposed by TVERGAARD [22]. It was found in [22] that this fibre arrangement gives a better agreement with experimental uniaxial stress-strain curves found by CHRISTMAN *et al.* [23] than that obtained by considering a simpler cell model representing transversely aligned fibres. The square array of fibres shown in Fig. 1b has the fibre spacing $2a_c$, and the initial radius $r_c = (2/\sqrt{\pi})a_c$ of the axisymmetric model is chosen such that the fibre volume fraction $f$ of the cell is equal to that of the material in Fig. 1

$$f = \frac{r_f^2 \ell_f}{r_c^2 \ell_c} \tag{2.1}$$

Here, $\ell_f$ and $r_f$ are the fibre half-length and radius, respectively, $\ell_c$ is the cell length, and the aspect ratios of the fibre and cell are

$$\alpha_f = \ell_f / r_f, \qquad \alpha_c = \ell_c / r_c. \tag{2.2}$$

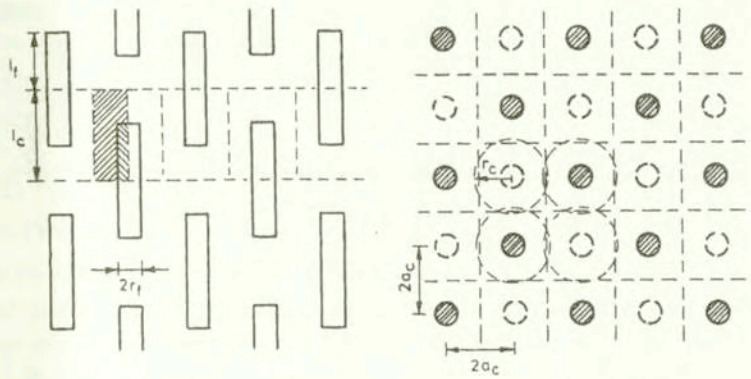


FIG. 1. Periodic array of aligned, transversely staggered fibres. a) cross-section along fibres; b) cross-section normal to fibres.

The major average principal stress $\sigma_1$ in the composite is taken to be in the axial direction, and due to the assumed axisymmetry only the cases with a uniform transverse average stress $\sigma_2$ can be considered. In the cases to be analysed, a fixed ratio between the axial and transverse average stresses is assumed

$$\sigma_2 = \rho \sigma_1. \tag{2.3}$$

The boundary conditions at the flat ends of the unit cell are straightforward, but on the curved side of the circular cylindrical cell, equilibrium and compatibility with the neighbouring cells has to be represented approximately. As is seen in Fig. 1a, a neighbouring cell is identical to that analysed, but points in the opposite direction. The detailed formulation of these boundary conditions can be found in TVERGAARD [22].

In the following analyses the matrix is modelled by the cyclic plasticity model with fatigue damage, while the fibres are taken to be elastic with Young's modulus $E_f$ and Poisson's ratio $\nu_f$. Furthermore, perfect bonding is assumed between the matrix and fibres, and the possibility of fibre fracture is neglected. Thus, the only type of failure accounted for is the fatigue damage evolution incorporated in the cyclic plasticity law used for the matrix.

The analyses in the present work are based on a small strain formulation of the field equations, since the geometry changes are typically small in fatigue situations, even though the accumulated plastic strain $p$ can grow large. The total strain increment is given by the sum of the elastic and plastic parts, $\dot{\epsilon}_{ij} = \dot{\epsilon}^e_{ij} + \dot{\epsilon}^p_{ij}$. The elastic stress-strain relationship is described by Hooke's law as $\dot{\sigma}_{ij} = L_{ijkl}\dot{\epsilon}^e_{kl}$, where the summation convention is adopted for repeated indices, $\sigma_{ij}$ is the stress tensor, and the elastic constants for the matrix denoted $E$ and $\nu$.

The plastic strain increment follows the normality rule, $\dot{\epsilon}^p_{ij} = \dfrac{\partial f}{\partial \sigma_{ij}}\dot{\lambda}$, where the plastic multiplier, $\dot{\lambda}$, is obtained from the consistency condition, $\dot{f} = 0$. A Mises yield surface with mixed hardening is used, as specified by

$$f = \tilde{\sigma}_e - (R + k) = 0, \tag{2.4}$$

where the stress state is described by the effective stress tensor, $\tilde{\sigma}_e = (3\tilde{s}_{ij}\tilde{s}_{ij}/2)^{1/2}$, in terms of the effective stress deviator $\tilde{s}_{ij} = \tilde{\sigma}_{ij} - \dfrac{1}{3}\delta_{ij}\tilde{\sigma}_{kk}$. Here, $\tilde{\sigma}_{ij} = \sigma_{ij}/(1 - D) - X_{ij}$, where $D$ is a scalar describing the amount of damage in a material point (LEMAITRE [18]). The kinematic hardening is governed by the back-stress tensor, $X_{ij}$, representing the centre of the yield surface in the stress space.

The size of the yield surface is described by the scalars $R$ and $k$. Here, $k$ is a constant and $R$ a variable, which is used for describing the isotropic hardening or softening of the material. The initial conditions of a cyclic hardening material are described by $k = \sigma_y$ and $R = 0$, where $\sigma_y$ denotes the initial yield stress. The evolution equation for the variable $R$ is described as

$$\dot{R} = b(R_\infty(\Lambda, q) - R)\dot{\lambda}, \tag{2.5}$$

where $b$ is a material parameter and the value $R_\infty(\Lambda, q)$ represents the limit of isotropic hardening or softening, as described in more detail in [24, 25]. The influ-

ence of the nonproportionality of the loading path on the softening or hardening of the material is described as suggested by BENALLAL *et al.* [26].

The kinematic hardening of the material is described by means of the back-stress tensor, $X_{ij}$, which is taken to be the sum of three contributions, in order to enhance the description of the material stress-strain response

$$X_{ij} = \sum_{n=1}^{3} X_{ij}^{(n)}. \tag{2.6}$$

Each of the back-stress tensors, $X_{ij}^{(n)}$, follow an evolution equation suggested in [16], and modified in [27] to enhance the description of ratchetting. The evolution equation for the back-stress deviator $X_{ij}^{D}$ is of the form

$$\dot{X}_{ij}^{D(n)} = \frac{2}{3}\gamma^{(n)} X_{\infty}^{(n)} \dot{\epsilon}_{ij}^{p} - \left[\frac{X_e^{(n)}}{X_{\infty}^{(n)}}\right]^{m_n} X_{ij}^{D(n)} \gamma^{(n)} \dot{\lambda}, \tag{2.7}$$

where the effective back-stress is $X_e^{(n)} = \left(\frac{3}{2} X_{pq}^{(n)} X_{pq}^{(n)}\right)^{1/2}$. The parameters in (2.7) and the representation of ratchetting are further described in [20, 12].

The scalar, $D$, which is incorporated in the constitutive equations as outlined by LEMAITRE [18], is used to describe the development of fatigue damage in the material. For an undamaged virgin material, $D = 0$, but when the accumulated plastic strain, $p$, reaches a threshold value $p_d$, damage starts developing in the sense of microvoids or microcracks. As it reaches a critical value $D_c$, the material has a high density of microcracks, which are likely to coalesce into a macrocrack leading to failure of the structural component. The damage development is described by

$$\dot{D} = \frac{Y}{S} \dot{p} \alpha(p), \qquad \alpha = \begin{cases} 1, & \text{if } p \geq p_d \\ 0, & \text{if } p < p_d \end{cases} \tag{2.8}$$

where $S$, is a material parameter describing the energy strength of damage. The effective plastic strain increment is determined as $\dot{p} = \left(\frac{2}{3}\dot{\epsilon}_{ij}^{p}\dot{\epsilon}_{ij}^{p}\right)^{1/2}$, which gives $\dot{p} = \dot{\lambda}/(1-D)$. The strain energy release rate is given by $Y = \sigma_e^2 R_V/(2E(1-D)^2)$, where the effective stress is denoted by $\sigma_e$, and the triaxiality of the stress field is accounted for by the parameter $R_V$, which is here taken to be specified by

$$R_V = \begin{cases} 1 + C\dfrac{\sigma_{kk}}{\sigma_y}, & \sigma_{kk} \geq 0, \\ \exp\left(C\dfrac{\sigma_{kk}}{\sigma_y}\right), & \sigma_{kk} < 0. \end{cases} \tag{2.9}$$

The material parameter $C$ is adjusted to describe the mean stress sensitivity of fatigue damage development [19], such that fatigue is more pronounced under tensile loading than under compressive loading.

The gradual formation of a crack in the matrix material around fibres, as the damage parameter $D$ reaches the critical value $D_c$, is described here by using a numerical techinque. In the previous investigations [12, 13] by the authors, only the initial stages of damage development were considered, so that the peak value of $D$ had not exceeded $D_c$.

The form of the incremental constitutive relations resulting from this material description for cyclic plasticity with fatigue damage has been given in detail in [12]. This material model for the metal matrix has as many as 23 material parameters, which have to be determined by experiments for the matrix material. Among these, $E$ and $\nu$ are the elastic constants, while $S$, $p_d$, $D_c$ and $C$ characterize the damage evolution, and the remaining 17 parameters are used to describe cyclic plastic deformations, including the Bauchinger effect, cyclic hardening or softening, ratchetting, and mean stress relaxation. Cyclic plasticity is complex and these many parameters are necessary to give an adequate description, as has been explained in a number of the papers cited above.

Numerical solutions are obtained by a finite element approximation, using a linear incremental method based on the principle of virtual work, as explained in [12]. An example of a mesh used for one of the numerical analyses is shown in Fig. 2, with the hatched region representing the fibre. The mesh consists of quadrilaterals, each built up of four crossed triangular elements with linear displacement assumption. A special Rayleigh-Ritz finite element method [28] is used to implement the boundary conditions and to enforce the fixed stress ratio (2.3).

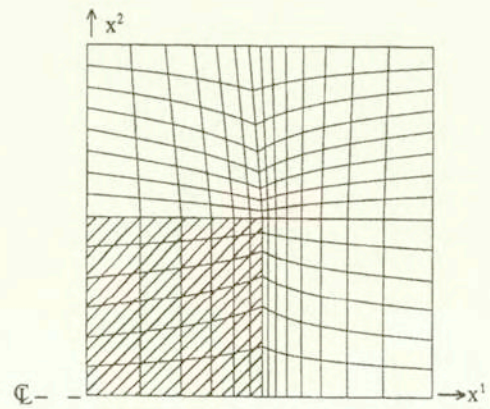


FIG. 2. Mesh used for some of the numerical computations.

The fatigue crack development is incorporated in the computations by using an element vanish technique [29]. Thus, when $D = D_c$ is reached in a triangular element, the stiffnes matrix for this element is set to zero, and the nodal forces corresponding to the remaining stresses in the element are stepped down to zero over a number of subsequent increments.

## 3. Results

The material values used here to represent the aluminium matrix are $k/E = 0.002$ and $\nu = 0.33$, and $b = 7.0$, $R_{\infty,s}/E = 0.012$, $R_0/E = 0$, $\alpha_R = 0.3$, $\beta_R = 160$, $\gamma_R = 0.5$ and $C_q = 0.5$. Furthermore, in the back-stress evolution equations (2.6) - (2.7), the parameter values used are $\gamma^1 = 400$, $\gamma^2 = 50$, $\gamma^3 = 2000$, $X^1_\infty/E = 0.0008575$, $X^2_\infty/E = 0.00142$, $X^3_\infty/E = 0.000285$, $m_1 = 3$, $m_2 = 3$ and $m_3 = 3$, as in [12]. In the damage evolution equations (2.8) - (2.9), the parameter values are $S/E = 0.000024$, $p_d = 0.03$, $D_c = 0.12$ and $C = 0.04$. Furthermore, the elastic constants of the SiC fibres are specified by $E_f/E = 5.71$ and $\nu_f = 0.21$ (see TEPLY and DVORAK [30]). For a rather soft aluminium most of the parameters needed in the cyclic plasticity model have been specified by HOPPERSTAD [31]. These values are used here, but the values of $k$ and the parameters specifying the kinematic hardening have been modified to better represent the aluminium with higher hardness used by CHRISTMAN *et al.* [23]. Furthermore, while HOPPERSTAD [31] used 2 terms in the sum (26), 3 terms are used here to obtain a more smooth transition from elastic to elastic-plastic deformation. The values of $S$, $p_d$ and $D_c$ are partly based on data given by LEMAITRE [18], and finally the value of $C$ is chosen to be reasonably representative of the measured mean stress dependence for high cycle fatigue of aluminium.

Figure 3 shows the overall stress-strain loops predicted for a particulate reinforced material with the aspect ratios $\alpha_f = \alpha_c = 1$ and the fibre volume fraction $f = 0.13$. Here a uniaxial cyclic stress is prescribed, $\rho = 0$, using stress-controlled loading with balanced cycling, $\sigma_{\max}/E = -\sigma_{\min}/E = 0.0036$. In this kind of test, strain ratchetting is possible and is in fact often observed [8], as has been discussed in [12]. In Fig. 3, where 27 loops have been reached, the first several loops show a slow movement of the mean strain in the negative direction, i.e. some ratchetting due to the hardening behaviour. But the most significant feature of this figure is the result of final failure development, which gives much larger strain amplitudes in the last loop, and also significantly reduced slopes on the elastic parts of this loop. Towards the end, the stress-strain curve is somewhat jumpy as a result of the gradual failure evolution, which is represented in the solution by using the element vanish technique.

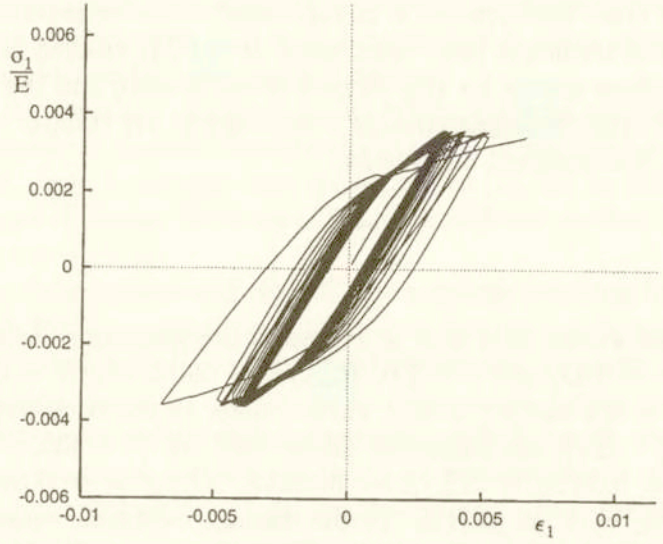


FIG. 3. Overall stress-strain loops for 27 cycles with balanced stress-controlled cycling, $\sigma_{\max}/E = -\sigma_{\min}/E = 0.0036$. Here, $f = 0.13$, $\alpha_f = \alpha_c = 1$ and $\rho = 0$.

Figure 4 shows the distribution of damage at two stages of the solution, i.e. for $\epsilon_1 = -0.0013$, $\sigma_1/E = -0.0019$, during loop No. 22, and for $\epsilon_1 = 0.0060$, $\sigma_1/E = 0.0034$, during loop No. 27, just near the end of the curve shown in Fig. 3.

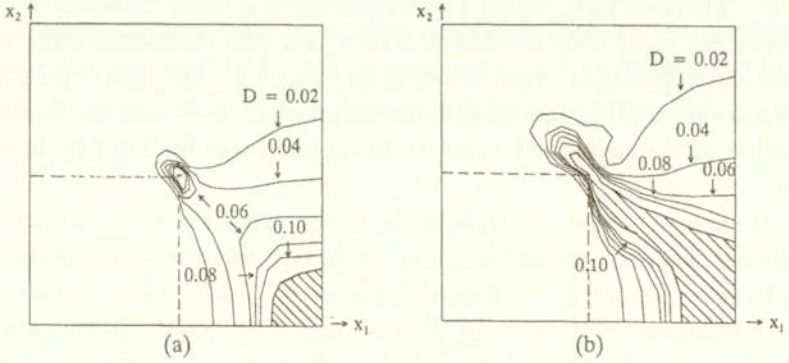


FIG. 4. Contours of constant damage, for balance stress-controlled loading, $\sigma_{\max}/E = -\sigma_{\min}/E = 0.0036$, with $f = 0.13$, $\alpha_f = \alpha_c = 1$ and $\rho = 0$. a) at $\epsilon_1 = -0.0013$, $\sigma_1/E = -0.0019$, during loop No. 22; b) at $\epsilon_1 = 0.0060$, $\sigma_1/E = 0.0034$, during loop No. 27.

The distributions of damage $D$ are shown by the contour curves, and regions where final failure has occured are shown hatched. The location of the particulate is indicated by dashed lines, and it should be noted that the apparent small amount of damage inside the sharp fibre edge is due to a plotting inaccuracy

resulting from averaging in the plotting programme. The distribution of the damage fields is quite similar to the results shown in [12], but the present results are extended to also show the onset of final failure in the matrix material and the subsequent crack growth. Figure 4a shows that failure has first developed at the axis of the cylindrical cell, centrally between two fibre ends, while failure at the sharp fibre edge is just initiating. In Fig. 4b these two failure regions have grown together, forming a crack that significantly reduces the strength of the cell, as is also seen in the last loop of the stress-strain curve in Fig. 3.

Figures 5 and 6 show analogous results for a larger particle volume fraction, $f = 0.35$, with the same values of the material parameters for the matrix and particles. The larger stiffness due to the higher reinforcement volume fraction results in a smaller overall strain range corresponding to the same stress amplitudes. Here, 70 loops have been reached, and the end of the curve shows that final failure is developing under monotonic elongation, without reaching the prescribed tensile stress amplitude in this last loop. The damage distributions in Fig. 6 correspond to two rather late stages, at $\epsilon_1 = 0.00041$, $\sigma_1/E = 0.00067$, during loop No. 67, and at $\epsilon_1 = 0.0052$, $\sigma_1/E = 0.0026$, during loop No. 70. In Fig. 6a only a tiny region of final failure has developed at the sharp particulate edge, but there is a high level of damage in a large material region at the plane of symmetry between two particle ends. Just three loops later Fig. 6b shows that much material has failed completely, and that the two open cracks have nearly linked up.

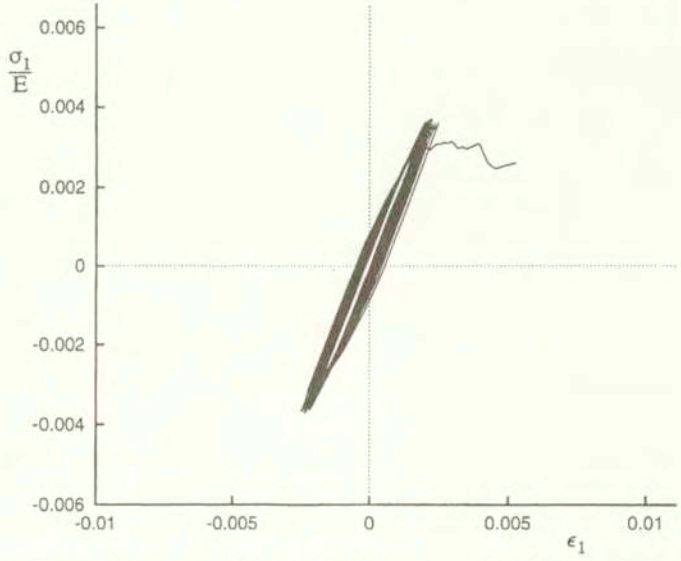


FIG. 5. Overall stress-strain loops for 70 cycles with balanced stress-controlled cycling, $\sigma_{\max}/E = -\sigma_{\min}/E = 0.0036$. Here, $f = 0.35$, $\alpha_f = \alpha_c = 1$ and $\rho = 0$.

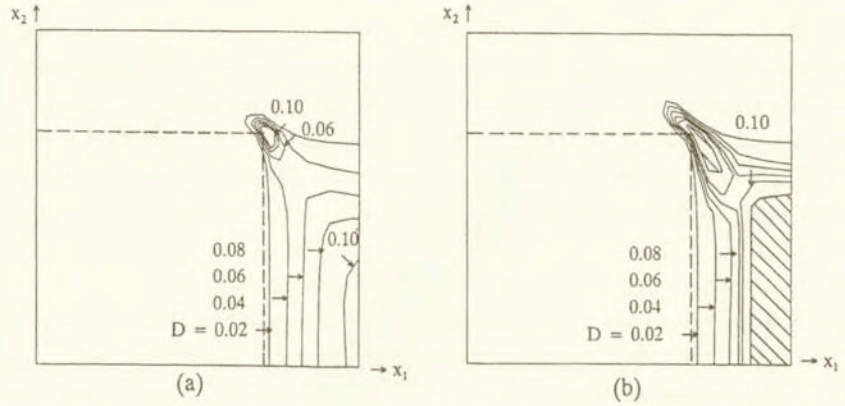


FIG. 6. Contours of constant damage, for balanced stress-controlled loading, $\sigma_{\max}/E = -\sigma_{\min}/E = 0.0036$, with $f = 0.35$, $\alpha_f = \alpha_c = 1$ and $\rho = 0$. a) at $\epsilon_1 = -0.00041$, $\sigma_1/E = 0.00067$, during loop No. 67; b) at $\epsilon_1 = 0.0052$, $\sigma_1/E = 0.0026$, during loop No. 70.

It is noted that the last part of the overall stress-strain curve shown in Fig. 5 would not be stable if a monotonically increasing load was prescribed. In the computations it has been assumed that a low constant strain rate is prescribed (for quasi static behaviour), and that the sign of the strain rate is reversed when the prescribed overall stress amplitude has been reached.

Again for the same values of the material parameters and stress amplitudes, and for $f = 0.13$ as in Figs. 3 and 4, results for higher aspect ratios of the fibre and the unit cell, $\alpha_f = \alpha_c = 2$, are shown in the next two figures. As expected, the longer fibres give higher overall stiffness, which leads to a somewhat smaller overall strain range than that found in Fig. 3, but the stress-strain loops in Fig. 7 still show clearly that the slopes are reduced in the last loop, due to the failure evolution. The damage field at a stage near the end of the solution, at $\epsilon_1 = 0.0039$, $\sigma_1/E = 0.0030$, during loop No. 27 (i.e. the last loop), is illustrated in Fig. 8. Here, the region of final failure has initiated at the sharp fibre, edge, and is currently extended on both sides of this point. It is seen that the maximum damage level along the axis of the cylindrical cell had been reached about one fibre radius ahead of the fibre end, but that the region of final failure is closer to the flat fibre end than indicated by the initial damage distribution.

Also a case of still larger aspect ratios, $\alpha_f = \alpha_c = 4$, has been analysed under the same balanced uniaxial cyclic stress. This gives still more narrow hysteresis loops, more like those shown in Fig. 5. Here, we only show the damage fields and the distribution of final failure in Fig. 9, at $\epsilon_1 = 0,0025$, $\sigma_1/E = 0.0028$, during loop No. 29 (the last loop). This figure shows that the failure distribution near the end of the longer fibre is very similar to that found for $\alpha_f = \alpha_c = 2$.

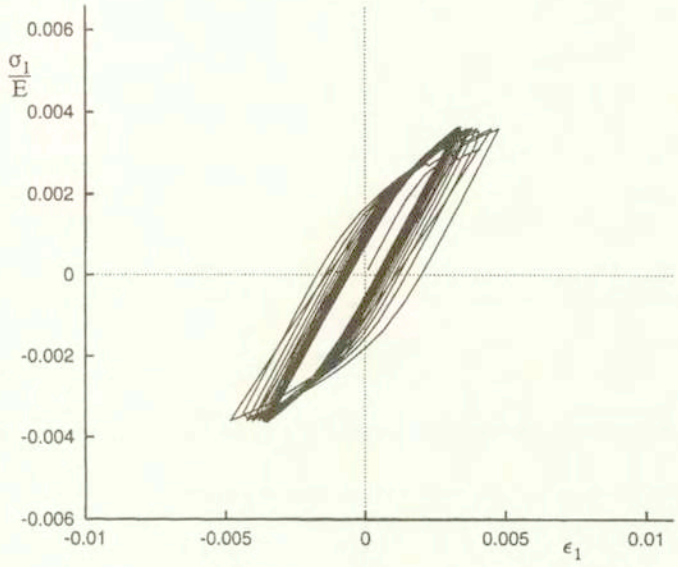


FIG. 7. Overall stress-strain loops for 27 cycles with balanced stress-controlled cycling, $\sigma_{\max}/E = -\sigma_{\min}/E = 0.0036$. Here, $f = 0.13$, $\alpha_f = \alpha_c = 2$ and $\rho = 0$.

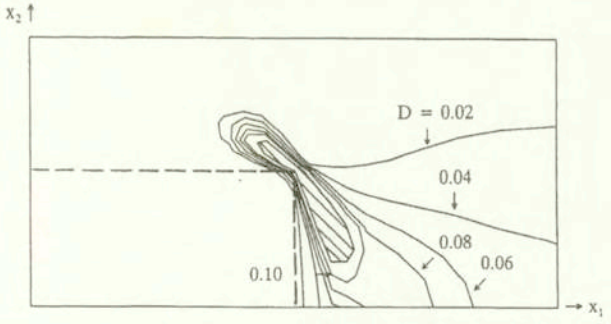


FIG. 8. Contours of constant damage, for balanced stress-controlled loading, $\sigma_{\max}/E = -\sigma_{\min}/E = 0.0036$, with $f = 0.13$, $\alpha_f = \alpha_c = 2$ and $\rho = 0$. At $\epsilon_1 = 0.0039$, $\sigma_1/E = 0.0030$, during loop No. 27.

The effect of stress triaxiality is considered in Figs. 10 and 11, where transverse tension is specified by $\rho = \sigma_2/\sigma_1 = 0.25$ The material is the same as that studied in Figs. 7 and 8, with $\alpha_f = \alpha_c = 2$, but higher stress amplitudes are used here, $\sigma_{\max}/E = -\sigma_{\min}/E = 0.0048$, since an important effect of the increased stress triaxially is that higher stress levels are required to give plastic yielding. The stress-strain loops in Fig. 10 show the same trends at those found in the previous cases, under cyclic uniaxial stress. Thus, the strain range is gradually reduced in the first cycles due to the hardening behaviour, and some ratchetting in the negative direction takes place, while in the last loops the strain range

increases again, due to the evolution of damage and final failure in the matrix material. Figure 11 shows the damage fields and the region of final failure in the last loop (i.e. in loop No. 17), at $\epsilon_1 = 0.0032$, $\sigma_1/E = 0.0039$. It is seen that the failure distribution here is rather similar to that shown in Fig. 8.

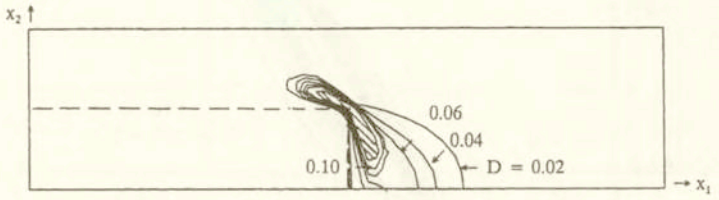


FIG. 9. Contours of constant damage, for balanced stress-controlled, $\sigma_{\max}/E = -\sigma_{\min}/E = 0.0036$, with $f = 0.13$, $\alpha_f = \alpha_c = 4$ and $\rho = 0$. At $\epsilon_1 = 0,0025$, $\sigma_1/E = 0.0028$, during loop No. 29.

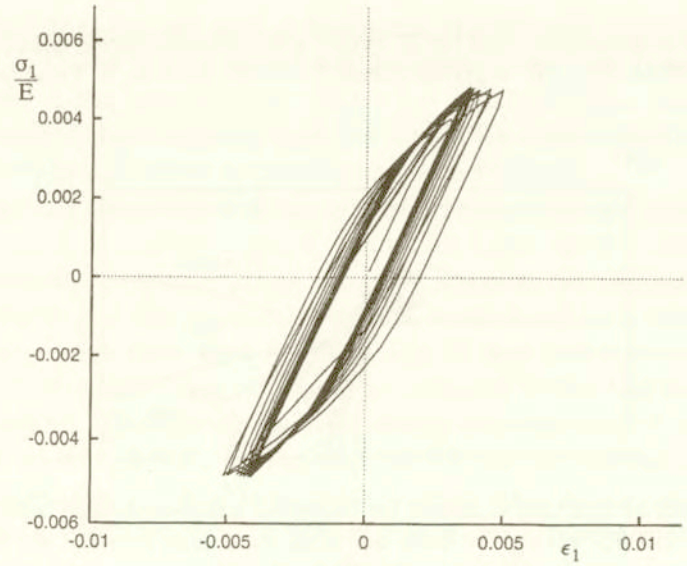


FIG. 10. Overall stress-strain loops for 17 cycles with balanced stress-controlled cycling, $\sigma_{\max}/E = -\sigma_{\min}/E = 0.0048$. Here, $f = 0.13$, $\alpha_f = \alpha_c = 2$ and $\rho = 0.25$.

Also strain-controlled cycling is important in applications and in test situations. A few cases have been analysed here for uniaxial stress conditions, i.e. for $\rho = 0$ in (2.3). For $(\epsilon_1)_{\max} = -(\epsilon_1)_{\min} = 0.004$, stress-strain loops for the material with $f = 0.13$ and $\alpha_f = \alpha_c = 1$ are shown in Fig. 12. The first loops are very similar to those in Fig. 3, but due to the fixed strain amplitude, the cyclic hardening here results in gradually increasing stress amplitudes. Later on, as damage results in the growth of a crack through the matrix, the material

stiffness is reduced, and then the fixed strain amplitude results in significantly reduced stress amplitudes, as is seen for the last loops in Fig. 12. The corresponding development of low-cycle fatigue is illustrated in Fig. 13 for an intermediate stage at $\epsilon_1 = -0.0011$, $\sigma_1/E = -0.00035$, in loop No. 17, and for the last loop analysed (loop No. 64) at $\epsilon_1 \simeq 0$, $\sigma_1/E = -0.00013$. The fields in Fig. 13a are rather similar to those in Fig. 4a, although the situation in Fig. 13a is slightly before the first onset of final failure. Figure 13b shows a very well-developed crack, close to a situation where the fibres are completely separated from parts

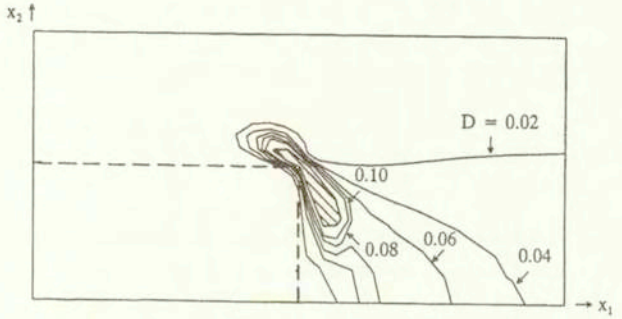


FIG. 11. Contours of constant damage, for balanced stress-controlled loading, $\sigma_{max}/E = -\sigma_{min}/E = 0.0036$, with $f = 0.13$, $\alpha_f = \alpha_c = 2$ and $\rho = 0.25$. At $\epsilon 1 = 0.0032$, $\sigma_1/E = 0.0039$, during loop No. 17.

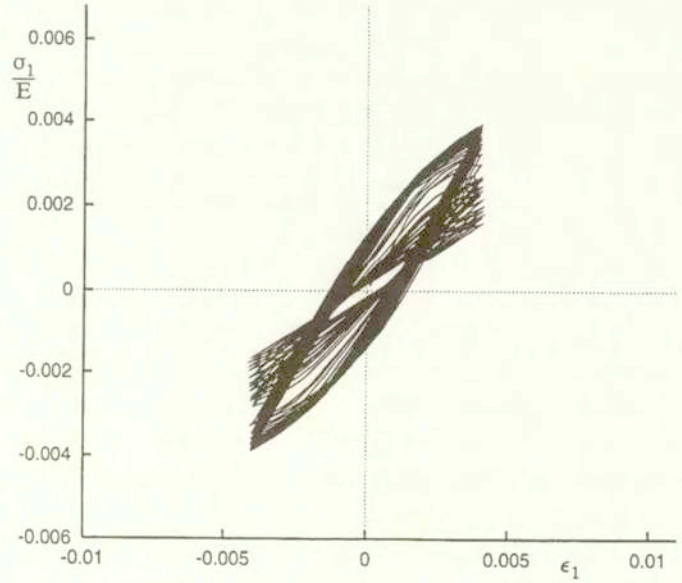


FIG. 12. Overall stress-strain loops for 64 cycles with balanced strain-controlled cycling, $(\epsilon_1)_{max} = -(\epsilon_1)_{min} = 0.004$. Here, $f = 0.13$, $\alpha_f = \alpha_c = 1$ and $\rho = 0$.

of the matrix material. Similar analysed for a material with $\alpha_f = \alpha_c = 2$ (as that in Figs. 7 and 8) has shown a behaviour analogous to that found in Fig. 12 and 13.

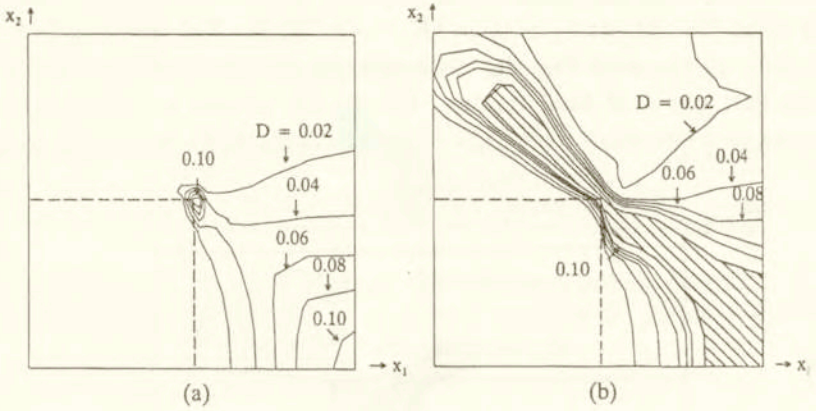


FIG. 13. Contours of constant damage, for balanced strain-controlled loading, $(\epsilon_1)_{\max} = -(\epsilon_1)_{\min} = 0.0036$, with $f = 0.13$, $\alpha_f = \alpha_c = 1$ and $\rho = 0$. a) at $\epsilon_1 = -0.0011$, $\sigma_1/E = -0.0035$, during loop No. 17; b) at $\epsilon_1 \simeq 0$, $\sigma_1/E = -0.00013$, during loop No. 64.

## 4. Discussion

Previous studies of the damage evolution by fatigue failure in metal matrix composites have been extended here to also account for the final failure of the matrix material and the subsequent growth of a matrix crack. The onset of failure is controlled by the damage model, as the failure criterion relies on reaching a critical value of the damage parameter, and the numerical representation of final failure applied here has made it possible to continue the fatigue analyses far beyond the initial stages of damage evolution.

In should be emphasized that the metal matrix fatigue failure investigated here is only one of the failure mechanisms observed for MMC's (ALLISON and JONES [8]), and that also fibre fracture and debonding of the fibre-matrix interface play a role in practice. But there is a wide range of cyclic loads for which the matrix fatigue characteristics dominate the fatigue life, and for this range of material behaviour the method presented here is expected to be a very useful tool in parametric studies of the effect of the main parameters characterising the metal matrix composite.

The examples used to illustrate the method here are all in the range of low cycle fatigue, since the number of cycles to final failure range from 17 to 70. This choice has been made for convenience, to avoid very large numbers of cycles in the numerical computations. However, since the predicted fatigue damage evolution

is linked to the amount of plastic straining, it is clear that somewhat smaller overall stress amplitudes will give much less plastic strain accumulation in each increment, and therefore a much increased number of cycles before final fatigue failure is predicted.

In comparing the analyses for fixed overall stress amplitudes and for a fixed fibre volume fraction, but with three different values, 1, 2 and 4, of the fibre and cell aspect ratios, it has been noted that increased fibre aspect ratio gives higher axial stiffness, and therefore a smaller overall strain range corresponding to the fixed stress range. But it is also noted that the number of cycles to final fatigue failure in these three cases is practically the same. This emphasizes the fact that the onset of final fatigue failure in the metal matrix is a function of local plastic strains rather than overall plastic strains. While increasing fibre length gives smaller overall strain range, it also results in larger local strain concentrations near the sharp edges at the fibre ends, and the final fatigue life determined in the numerical analyses is a result of competition between these two effects.

## References


1. A. NEEDLEMAN, S. R. NUTT, S. SURESH and V. TVERGAARD, *Matrix, reinforcement and interfacial failure*, Fundamentals of Metal Matrix Composites, S. SURESH *et al.* [Eds.], Butterworth-Heinemann, Boston, MA, 233–250, 1993.
2. S. R. NUTT and A. NEEDLEMAN, *Void nucleation at fiber ends in Al-SiC composites*, Scr. Metall., **21**, 705–710, 1987.
3. V. TVERGAARD, *Effect of fibre debonding in a whisker-reinforced metal*, Mater. Sci. Eng., **A 125**, 203–213, 1990.
4. V. TVERGAARD, *Model studies of fibre breakage and debonding in a metal reinforced by short fibres*, J. Mech. Phys. Solids, **41**, 1309–1326, 1993.
5. V. TVERGAARD, *Fibre debonding and breakage in a whisker-reinforced metal*, Mater. Sci. Eng., **A 190**, 215–222, 1995.
6. V. TVERGAARD, *Effects of ductile matrix failure in three dimensional analysis of metal matrix composites*, Acta Mater., **46**, 3637–3648, 1998.
7. J. LLORCA, A. NEEDLEMANN and S. SURESH, *An analysis of the effects of matrix void growth on deformation and ductility in metal-ceramic composites*, Acta Metall. Mater., **39**, 2317–2335, 1991.
8. J. E. ALLISON and J. W. JONES, *Fatigue behaviour of discontinously reinforced metal matrix composites*, Fundamentals of Metal Matrix Composites, S. SURESH *et al.* [Eds.], Butterworth-Heinemann, Boston, MA, 269–294, 1993.
9. J. LLORCA and P. POZA, *Influence of reinforcement fracture on the cyclic stress-strain curve of metal-matrix composites*, Acta Metall. Mater., **43**, 3959–3969, 1995.
10. J. LLORCA, S. SURESI and A. NEEDLEMANN, *An experimental and numerical study of cyclic deformation in metal-matrix composites*, Metall. Trans., **23a**, 919–934, 1992.
11. A. L. GURSON, *Continuum theory of ductile rupture by void nucleation and growth – I. Yield criteria and flow rules for porous ductile media*, J. Engng. Materials Technol., **99**, 2–15, 1977.

12. T. Ø. PEDERSEN and V. TVERGAARD, *On low cycle fatigue in metal matrix composites*, Int. J. Damage Mechanics, **9**, 154–173, 2000.

13. V. TVERGAARD and T. Ø. PEDERSEN, *Fatigue damage development in a steel based MMC*, Proc. 3rd National Congr. Comput. Mech., N. ARAVAS *et al.* [Eds.], University of Thessaly, Greece, 101–108, 1999.

14. J. F. BESSELING, *A theory of elastic, plastic, and creep deformations of an initially isotropic material showing anisotropic strain-hardening, creep recovery, and secondary creep*, J. Appl. Mech., **25**, 529–536, 1958.

15. Z. MRÓZ, *On the description of anisotropic workhardening*, J. Mech. Phys. Solids, **15**, 163–175, 1967.

16. P. J. ARMSTRONG and C. O. FREDERICK, *A mathematical representation of the multiaxial Bauschinger effect*, CEGB Report RD/B/N731, Berkeley Nuclear Laboratories, 1966.

17. J. LEMAITRE and J.-L. CHABOCHE, *Mechanics of Solids Materials*, Cambridge University Press, 1990.

18. J. LEMAITRE, *A Course on Damage Mechanics*, Springer-Verlag, 1992.

19. T. Ø. PEDERSEN, *Numerical modelling of cyclic plasticity and fatigue damage in cold-forging tools*, Int. J. Mechanical Sciences, **42**, 799–818, 2000.

20. T. Ø. PEDERSEN, *Numerical studies of low cycle fatigue in forward extrusion dies*, J. of Materials Processing Technology, 1999 (to appear).

21. H. S. NIELSEN and V. TVERGAARD, *Intergranular fracture under creep-fatigue interaction*, Int. J. Damage Mechanics, **7**, 3–23, 1998.

22. V. TVERGAARD, *Analysis of tensile properties for a whisker-reinforced metal-matrix composite*, Acta Metall. Mater., **38**, 185–194, 1990.

23. T. CHRISTMAN, A. NEEDLEMANN, S. NUTT and S. SURESH, *On microstructural evolution and micromechanical modelling of deformation of a whisker-reinforced metal-matrix composite*, Mat. Sci. Eng., **A107**, 49–61, 1989.

24. O. S. HOPPERSTAD, M. LANGSETH and S. REMSETH, *Cyclic stress-strain behaviour of alloy AA6060, Part I: Uniaxial experiments and modelling*, Int. Journal of Plasticity, **11**, 725–739, 1995.

25. J. L. CHABOCHE, *Time-independent consitutive theories for cyclic plasticity*, Int. Journal of Plasticity, **2**, 149–188, 1986.

26. A. BENALLAL, O. LE GALLO and D. MARQUIS, *Cyclic hardening of metals under complex loadings*, Proc. MECAMAT, Int. seminar on the inelastic behaviour of solids: models and utilisation (Besancon, France), 361–371, 1998.

27. N. OHNO and J.-D. WANG, *Kinematic hardening rules with critical state of dynamic recovery, Part I: Formulation and basic features for ratchetting behaviour*, Int. Journal of Plasticity, **9**, 375–390, 1993.

28. V. TVERGAARD, *Effect of thickness inhomogeneities in internally pressurized elastic-plastic spherical shells*, J. Mech. Phys. Solids, **24**, 291–304, 1976.

29. V. TVERGAARD, *Influence of void nucleation on ductile shear fracture at a free surface*, J. Mech. Phys. Solids, **30**, 399–425, 1982.

30. J. L. TEPLY and G. J. DVORAK, *Bounds on overall instantaneous properties of elastic-plastic composites*, J. Mech. Phys. Solids, **36**, 29–58, 1988.

31. O. S. HOPPERSTAD, *Modelling of cyclic plasticity with application to steel and aluminium structures*, Dr. Ing. Dissertation, Dept. of Structural Engineering, The Norwegian Inst. of Technology, Trondheim, Norway.

*Received January 31, 2000.*